nature physics

Article

https://doi.org/10.1038/s41567-023-02360-5

Hopping frustration-induced flat band and strange metallicity in a kagome metal

In the format provided by the authors and unedited

Supplementary Materials:
Hopping frustration-induced flat band and strange metallicity in a kagome metal

CONTENTS

SI. Structural characterization of Ni_3In

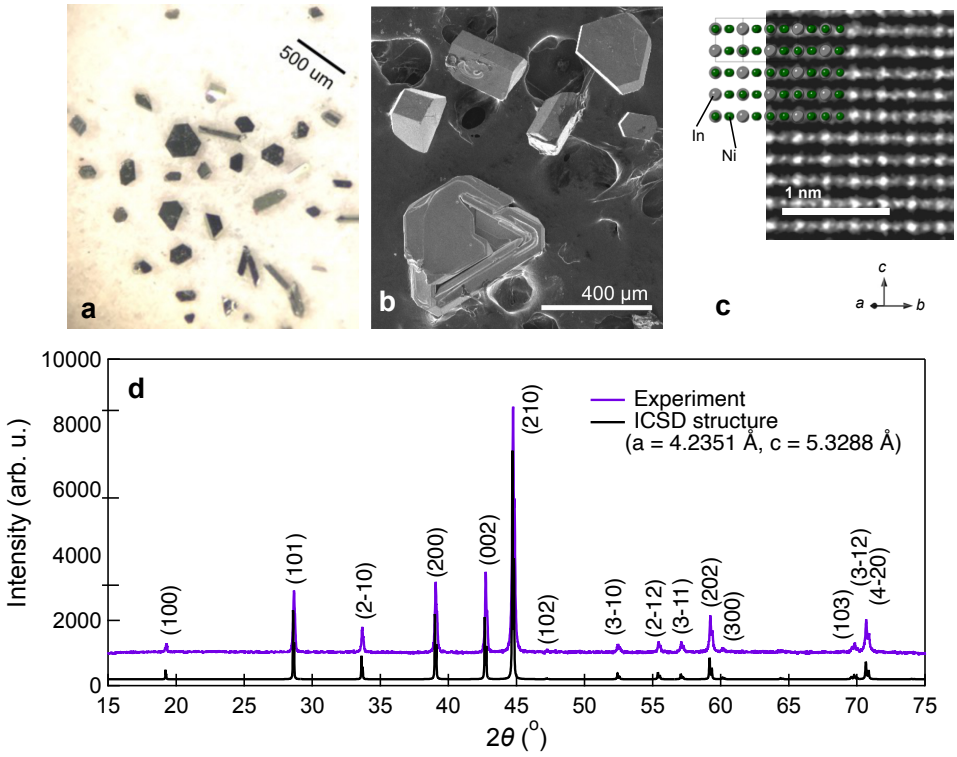

FIG. S1. **Structural characterization of Ni_3In** (a) Optical and (b) Scanning Electron Microscope (SEM) image of Ni_3In single crystals; the majority of the crystals are of a hexagonal prism morphology and exhibit metallic reflections. (c) Transmission Electron Miscroscopy (TEM) cross section view of single crystalline Ni_3In from the [210] orientation; the TEM pattern is partially overlaid with the crystal structure viewed from the same direction. (d) Powder X-ray diffraction pattern (purple) and theoretical XRD pattern; the latter is calculated from ICSD structure [S1] with lattice constants updated to fit the experimentally observed peak positions (a = 4.2351 Å, c = 5.3288 Å).

SII. Density functional theory analysis of the electronic structure of Ni_3In

The electronic structure of Ni_3In with and without spin-orbit coupling along the high symmetry lines are shown in green and black, respectively in Fig. S2. The energy position and the band width of the flat band are largely unaffected by the introduction of spin-orbit

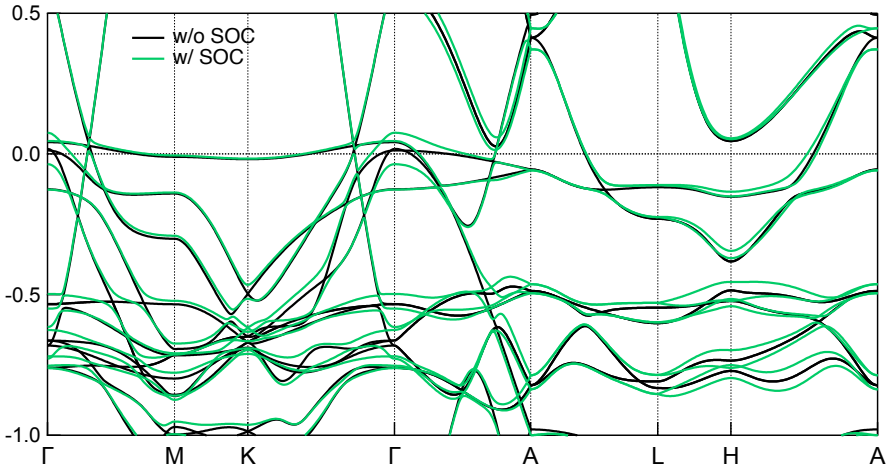

FIG. S2. **Band dispersions of Ni_3In** Density functional theory (DFT) band structure of Ni_3In along the high symmetry lines with (green) and without (black) spin-orbit coupling.

coupling apart from near the gap openings at the crossings between the highly dispersive bands and the flat band. We expand on the nature of this band crossing below. Close to $E = -0.5$ eV, we observe a Dirac-like crossing at K which is gapped by spin-orbit coupling similar to that previously seen in other kagome metals [S2]. The non-symmorphic symmetry of space group No. 194 ($P6_3/mmc$) requires the bands to be degenerate (in addition to the spin degeneracy) at the $k_z = \pi/c$ plane in the absence of spin-orbit coupling [S3]. With spin-orbit coupling only bands along $\mathrm{A} - \mathrm{L}$ are left bound in this fashion.

In the following we examine the nature of the crossing between the steep band dispersions close to the Fermi level E_F. In the non-relativistic band structure, the crossing point (Dirac nodes) are found to form a closed loop that lies in the $k_z = 0$ plane as illustrated in Fig. S3(a), which we refer to as "Dirac nodal ring" hereafter. Within the $k_z = 0$ plane, the wave vector on the nodal ring $k_{\mathrm{NR}} = (0.218 \pm 0.002)\,\text{Å}^{-1}$ appears isotropic with a weak six-fold variation with the polar angle ϕ as shown in Fig. S3(b). The nodal energy $E_{\mathrm{NR}} = (25 \pm 7)$ meV evolves with ϕ in a similar manner. We note that E_{NR} falls within the width of the flat band over the entire $k_z = 0$ plane so that we may view these nodes as degenerate with the flat band states. Without spin-orbit coupling, our analysis of the wave function suggests that the nodal ring is protected from gap opening due to the mirror symmetry of the $k_z = 0$ plane, as the electron-like and hole-like branches composing the nodal ring possess opposite mirror eigenvalues as shown in Fig. S3(c). The introduction of spin-orbit coupling opens a

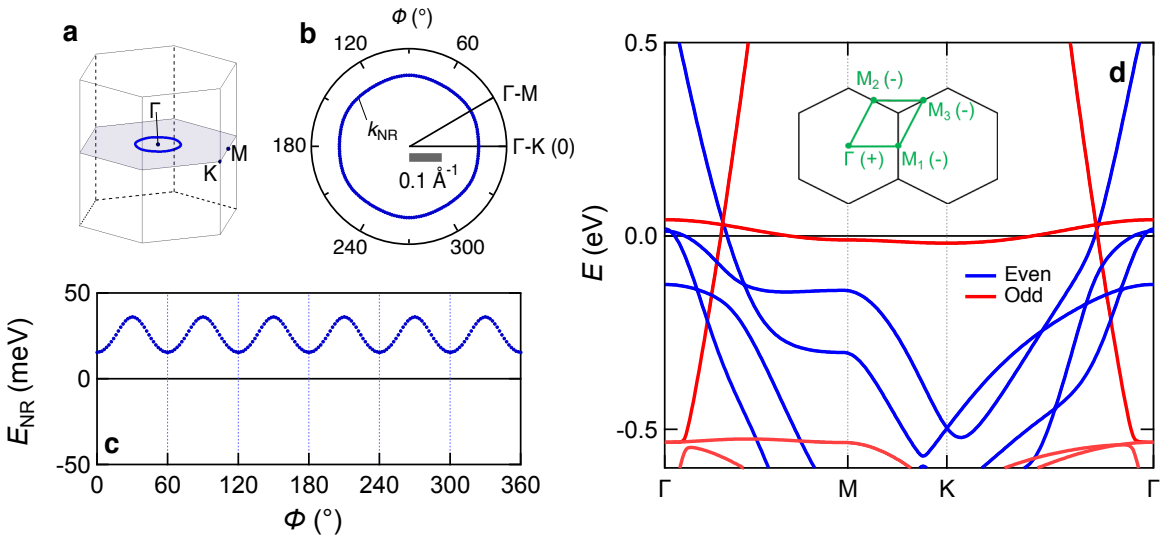

FIG. S3. **Analysis of the Dirac nodal ring in Ni_3In** (a) Location of the nodal ring (blue circle) in the Brillouin zone, where the translucent blue plane represents the $k_z = 0$ plane. (b) Top view of the nodal ring within the $k_z = 0$ plane and where the radial coordinate is the nodal ring wave vector k_{NR}. The polar angle ϕ is defined with respect to the $\Gamma-\mathrm{K}$ direction. (c) The evolution of the nodal energy E_{NR} with ϕ along the nodal ring. (d) The band dispersion without spin-orbit coupling labeled by the eigenvalue of the wave function under the xy-mirror operation. The red (blue) bands are odd (even) under the mirror operation. The inset depicts the time-reversal invariant momenta (green markers) Γ, M_1, M_2, M_3 with respect to the Brillouin zones (black hexagons); the corresponding products of parity eigenvalues at each momentum are also labeled.

topologically non-trivial gap on the order of 20 meV, as we verify the 2D Z_2 invariant $\nu = 1$ at the $k_z = 0$ plane via evaluating the parity eigenvalues of all filled bands at the time-reversal invariant momenta $\Gamma, \mathrm{M}_1, \mathrm{M}_2, \mathrm{M}_3$ (depicted schematically in Fig. S3(d) inset) [S4]. Similar action of spin-orbit coupling converting Dirac nodal rings into gapped topological insulating states has been suggested for a variety of nodal line semimetallic materials [S5]. Although a vanishing Fermi surface size of the nodal line states suggest that they contribute little to transport, it is intriguing to reveal the consequences of the hybridization of the nodal line states with the flat band.

To elucidate the origin of the unusual band structure figures of Ni_3In it is useful to examine the orbitally decomposed contributions of the electronic structure (shown in Fig.

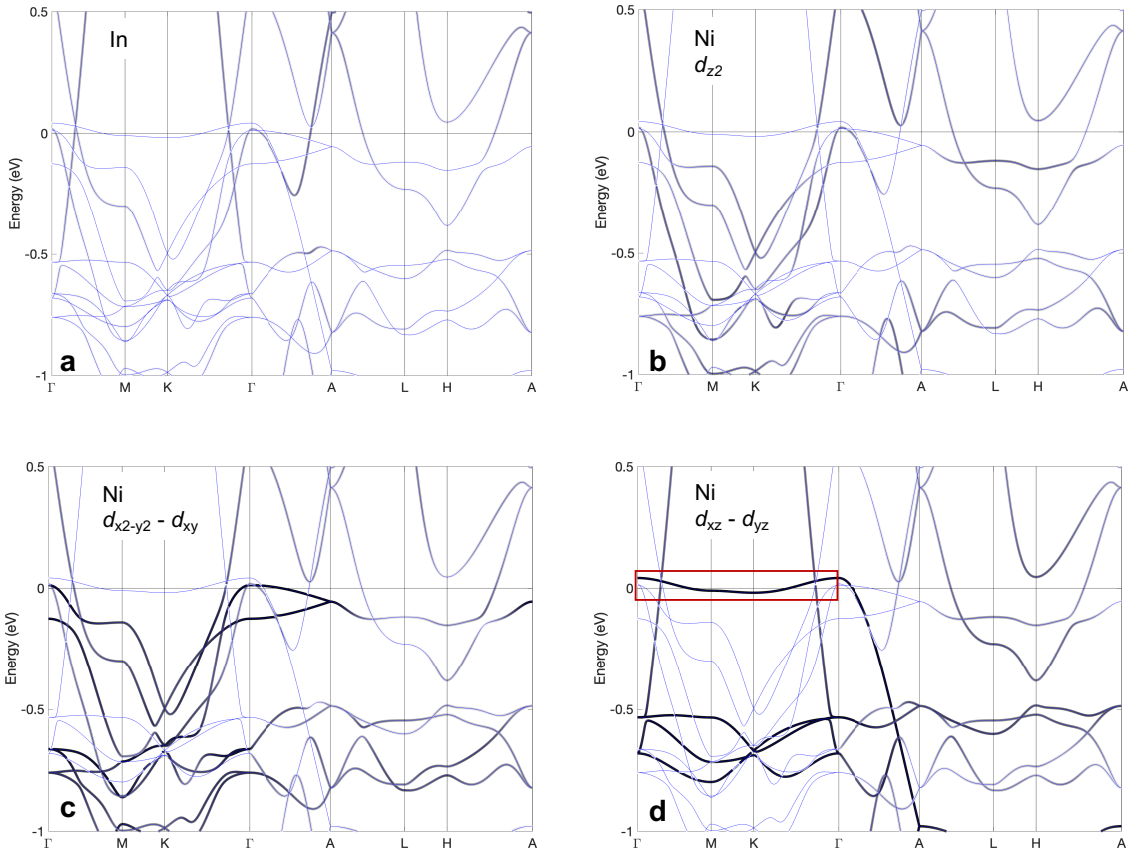

FIG. S4. **Orbital decomposition of the electronic structure** The band structure without spin-orbit coupling decomposed to (a) In (b) Ni $3d_{z^2}$ (c) $3d_{x^2-y^2} - d_{xy}$ and (d) $3d_{xz} - d_{yz}$ orbitals, respectively. The intensity in panel (a) is multiplied by a factor of three relative to (b)-(d) for clarity.

S4). For example, it becomes clear that the flat band at E_F arises primarily from the Ni $d_{xz} - d_{yz}$ states. The overall band structure of Ni_3In reflects several key features of the ideal kagome lattice (*e.g.* symmetry-protected band crossing at K near -0.6 eV) with a varying degree of dependence on k_z, which reflects the nature of the underlying d orbital (a locally rotated coordinate frame can be defined at each kagome site to further elucidate the local orbital orientations). We therefore note that the orbital degrees of freedom, together with the presence or absence of honeycomb spacer layers (*e.g.* stanene, germanene) between the kagome layers, are key factors for engineering the electronic dimensionality of kagome metals [S6].

SIII. Tight-binding modeling of the flat band in Ni_3In

To gain further insights into the flat band states from a DFT perspective, one may derive Wannier tight-binding models using proper basis states for the projection. We define them as the (full) *ab initio* Wannier tight-binding model and the numerical projections are implemented in the PYFPLO code. This complete model contains the $s/p/d$ orbitals of Ni and In as the basis states. As we show in the following, a small subset of basis states suffice to capture the near E_F states including the flat band features. We introduce two flavors of effective Wannier tight-binding models as such using either the atomic d_{xz} orbital state or the molecular orbital states at the cluster sites as their respective basis states.

a. Effective tight-binding model: atomic orbital basis

Motivated by the orbital configuration as illustrated in Fig. S5(a,b), we have constructed a tight-binding model on the bilayer kagome lattice with hopping parameters ranging from $t_0 - t_4$ shown in Fig. S5(c) to account for the six-band hopping based on the local d_{xz} orbital (in rotated coordinate) and to illustrate a possible mechanism for the reduced dispersion at the $k_z = 0$ plane. Among the hopping paths shown in Fig. S5(c) we take t_0 as the strongest hopping where the local d_{xz} orbital lobes show the most significant overlap (dashed line in Fig. S5(a)). The tight-binding bands in Fig. S5(d) are obtained with $t_0 = 1, t_1 = 0.5, t_2 = 0.3, t_3 = 0.2$, and $t_4 = -0.1$ and that in Fig. S5(e) with $t_0 = 1, t_1 = 0.5, t_2 = 0.3, t_3 = 0.2$, and $t_4 = -0.15$. Contrasting these with the DFT bands over the range of -2.5 eV to 0.5 eV in Fig. S5(f), our tight-binding model is able to reproduce the $k_z = 0$ flat dispersion and its strong k_z evolution, together with the band features within the energy range -1.7 eV ~ -1 eV on the $\mathrm{A} - \mathrm{L} - \mathrm{H} - \mathrm{A}$ plane. The wave function amplitude at Γ for the flat band is found to be uniform on all the sublattice sites, consistent with the Wannier function shown in Fig. S5(a,b). Through comparing the hopping parameter sets in Fig. S5(d) and (e), we note that the flat dispersion results primarily from an interference of the hopping parameters t_2 and t_4 with the bandwidth being $|t_2 + 2t_4|$. In our model, the opposite signs of inter-cluster hopping parameters t_2 and t_4 – resulted from the particular d-electron orbital texture – appear to play a central role in flattening the dispersion within the kagome lattice plane.

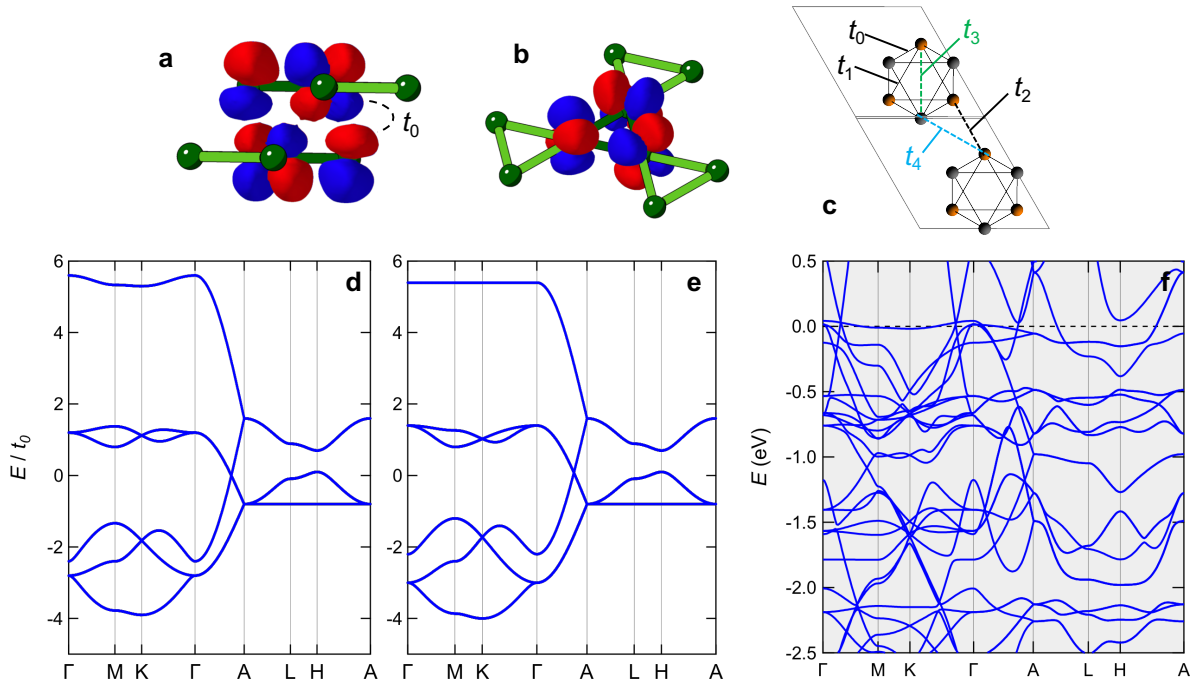

FIG. S5. **Tight-binding model of Ni_3In** (a,b) Wannier wave function of the flat band in $k_z = 0$ in a side view in (a) and a three-dimensional view in (b). The wave function with opposite sign is illustrated in red and blue. (c) Schematic of the hopping parameters $t_0 - t_4$ on the bilayer kagome model. Gray atoms are on the upper plane and orange atoms on the lower plane. The bonds within a cluster are highlighted with black solid lines. (d) Model band dispersion for $t_0 = 1, t_1 = 0.5, t_2 = 0.3, t_3 = 0.2$, and $t_4 = -0.1$. (e) Model band dispersion for $t_0 = 1, t_1 = 0.5, t_2 = 0.3, t_3 = 0.2$, and $t_4 = -0.15$. (f) DFT band structure without spin-orbit coupling from -2.5 eV to 0.5 eV.

b. Effective tight-binding model: molecular orbital basis

An alternative way of building an effective model is to use Wannier functions constructed from linear combinations of atomic orbitals with a particular orbital character. In contrast to the previous effective model, the new basis functions are molecular-like and their centers lie in between the respective atomic sites. A convenient choice is to construct such states for triangles of the kagome lattice (there are two types of triangles in the kagome lattice and the breathing mode breaks the symmetry; here we focus on the smaller triangle with shorter atomic distance). The main advantage is the reduction of the basis: since we are primarily interested in the d_{xz} and d_{xy} orbitals that dominate at the Fermi level, and a unit

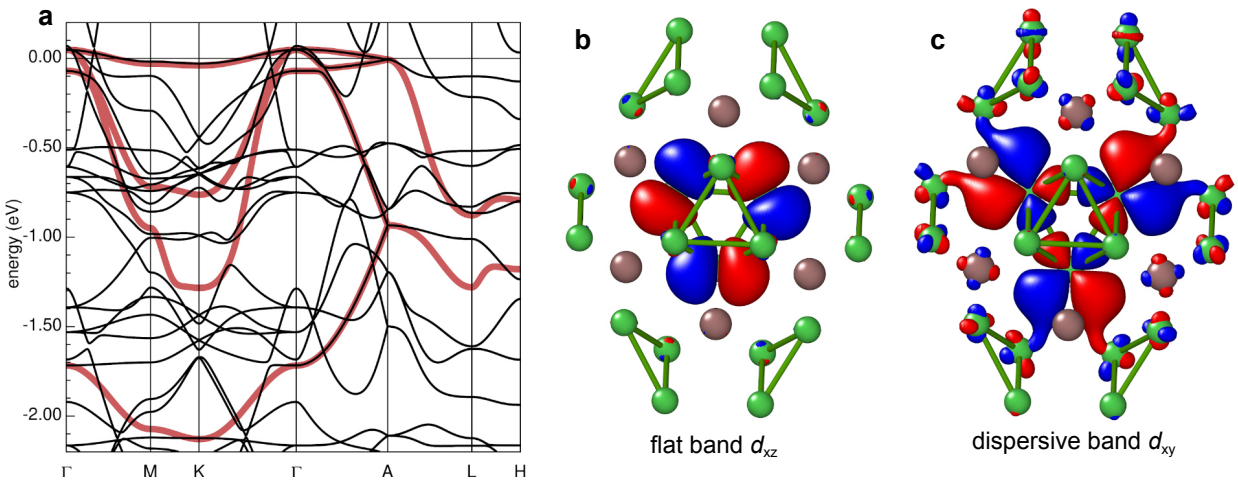

FIG. S6. **Effective model in the molecular-orbital basis** (a) GGA band structure of Ni_3In (thin lines) in comparison with Fourier-transformed Wannier Hamiltonian of the effective model in the molecular-orbital basis (thick lines). Each basis state of this model comprises a sum of atomic d_{xz} or d_{xy} orbitals (given in the local coordinate frame) of three Ni atoms forming a triangle in the kagome lattice. Real-space pictures of the Wannier states for the same isosurface value (0.12) reveal the spatial confinement (absence of sizable offsite contributions) of the xz states forming the flat band (b) in contrast to the xy states contributing to the dispersive band (c).

cell of Ni_3In contains two triangles, we can construct a minimal model with only four basis states. To this end, we choose the local coordinate system such that they are compatible with the symmetry elements of the space group. In this case, a sum of atomic contributions fulfills the symmetry requirements trivially (alternatively, it is possible to choose a common coordinate frame for all atoms and take the coefficients in the form of $e^{i\frac{n}{6}\pi}$ with $0 \leq n \leq 5$). This model provides an excellent description of the flat band along the $\Gamma-\mathrm{K}-\mathrm{M}-\Gamma$ path in Fig. S6(a) and of the dispersive bands along $\Gamma-\mathrm{A}$. Due to the minimal basis, it can neither account for the dispersive bands forming Dirac crossings, nor for the involved momentum dependence of the states deep in the valence band.

In Fig. S6(b,c), we plot these Wannier molecular orbital basis states in real space. There are two types: one comprising atomic d_{xz} orbitals and another comprising atomic d_{xy} orbitals. With the isovalue surface, we can see the distribution of electron densities. Comparing the two types of states, the local d_{xz} type is found to be more localized within the sites of a triangular cluster with almost no offsite contributions. This spatial localization is also con-

sistent with the destructive interference between hopping channels as discussed above which depends sensitively on the orbital types and orientations. In contrast, the local in-plane d_{xy} type has visible contributions on the neighboring atoms and beyond. The inter-cluster coupling controls the in-plane flat band dispersions in the electronic structure.

c. Ni_3In static susceptibility: numerical implementations

In this section, we discuss the calculations for Ni_3In static susceptibility based on the effective molecular orbital model derived above. For a single-band Hamiltonian $H(\vec{k})$, the non-interacting Green's function is given by

$$G^0(\vec{k}, i\omega_n) = \frac{1}{i\omega_n - H(\vec{k})}, \tag{S1}$$

where $\omega_n = \frac{(2n+1)\pi}{\beta}$ is the fermionic Matsubara frequency, with integers n and thermodynamic beta $\beta = (k_B T)^{-1}$. The momentum-dependent non-interacting magnetic susceptibility in imaginary time is given by the following Matsubara sum:

$$\chi^0(\vec{q}, ip_n) = -\frac{2\mu_B^2}{\beta}\frac{1}{N_{\vec{k}}}\sum_{\vec{k}, i\omega_n} G^0(\vec{k}, i\omega_n)G^0(\vec{k}+\vec{q}, i\omega_n + ip_n), \tag{S2}$$

where the bosonic Matsubara frequency $p_n = \frac{2n\pi}{\beta}$. The $\vec{k}$-summation can be replaced by averaging over the grid points sampled in the Brillouin zone. To relate to the static susceptibility in the real-time axis, one first performs the analytic continuation $ip_n \to \omega + i\eta$ and sets $\omega = 0$ for the static susceptibility. Numerically, this can be evaluated by first analytically computing the $i\omega_n$ sum and obtaining the expression in the real-time before setting $\omega = 0$. On the other hand, one could also directly evaluate numerically the $i\omega_n$ sum assuming $ip_n = 0$, in the imaginary time formalism. The two approaches (from real-time or imaginary-time axes) are equivalent since the analytic function at $\omega = 0$ is at the intersection of the real-time and imaginary-time axes. Below we give the numerical expressions for both formalisms when applied to the electronic structure computations.

For the effective models derived for the electronic structure of the materials, we have more than one site/basis state in the unit cell, and the Hamiltonian becomes a matrix $H_{ij}(\vec{k})$, as does the Green's function:

$$G^0_{ij}(\vec{k}, i\omega_n) = [i\omega_n \delta_{ij} - H_{ij}(\vec{k})]^{-1}. \tag{S3}$$

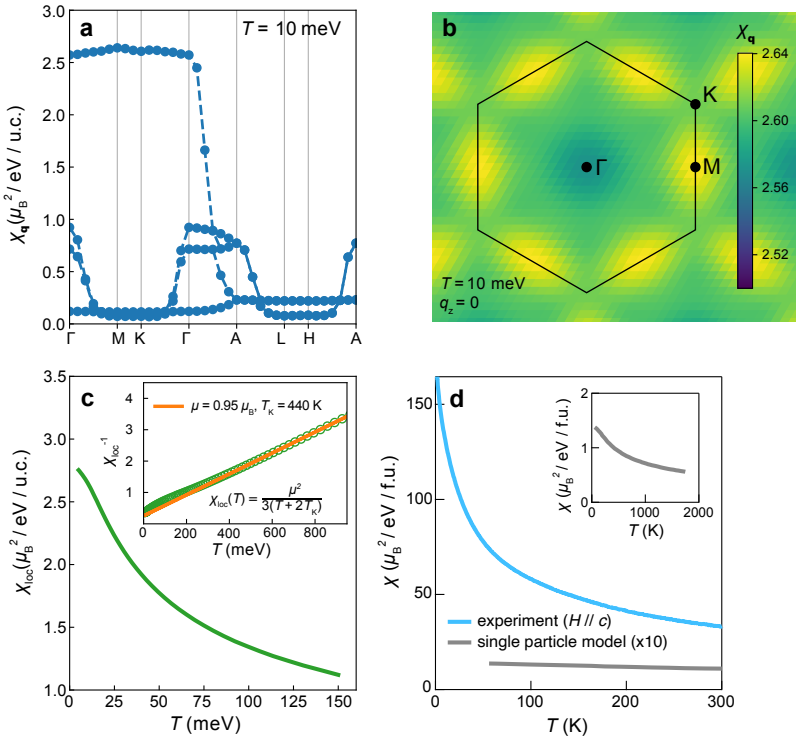

FIG. S7. **Ni_3In static susceptibility derived from the effective 4-band model** (a) The mode decomposition for $\chi^0_{\vec{q}}(\omega = 0)$ along a high symmetry line, by diagonalizing the $\chi^0_{\vec{q}}(\omega = 0)$ matrix, evaluated at $k_BT = 10$ meV. (b) The dominant mode $\max[\chi_{\vec{q}=(q_x,q_y,0)}]$ on the plane $q_z = 0$. (c) Temperature dependence of the static local susceptibility $\chi_{\rm loc}$ in the unit of μ_B^2/eV/unit cell. Inset shows a fit to the high-temperature part of $1/\chi_{\rm loc}$. (d) Comparison as a function of temperature of the calculated $\chi_{\rm loc}$ (gray curve) with the experimentally observed χ_c (blue curve) assuming a g-factor of 2. Note that here χ is shown in μ_B^2/eV per formula unit. Inset shows $\chi_{\rm loc}$ with temperature in the unit of Kelvin.

The susceptibility matrix is hence:

$$\chi^0_{ijkl}(\vec{q}, ip_n) = -\frac{2\mu_B^2}{\beta}\frac{1}{N_{\vec{k}}}\sum_{\vec{k},\omega_n} G^0_{il}(\vec{k}, i\omega_n)G^0_{jk}(\vec{k}+\vec{q}, i\omega_n + ip_n), \tag{S4}$$

and we would like to focus on the static $\chi^0_{ijij}(\vec{q}, ip_n \to 0 + i\eta)$ terms, which can be written out explicitly with the eigenstates and basis state expansions as:

$$\chi^0_q(\omega = 0) = -\frac{2\mu_B^2}{\beta}\sum_{k,i\omega_n}\sum_{\alpha_1,\alpha_2,i,j}\frac{\langle i|\psi^{\alpha_1}_k\rangle\langle\psi^{\alpha_1}_k|j\rangle\langle j|\psi^{\alpha_2}_{k+q}\rangle\langle\psi^{\alpha_2}_{k+q}|i\rangle}{(i\omega_n - \epsilon^{\alpha_1}_k)(i\omega_n + i\eta - \epsilon^{\alpha_2}_{k+q})}, \tag{S5}$$

where the Matsubara sum over $i\omega_n$ is carried out numerically in the imaginary-time axis while taking the static limit $ip_n \to 0 + i\eta$. The cutoff in the $i\omega_n$ sum is checked for convergence.

On the other hand, the Matsubara sum over $i\omega_n$ and analytic continuation to the real-time axis can be exactly derived, and gives

$$\chi_q^0(\omega) = 2\mu_B^2 \sum_k \sum_{i,j} \sum_{\alpha_1,\alpha_2} \frac{\langle i|\psi_k^{\alpha_1}\rangle\langle\psi_k^{\alpha_1}|j\rangle\langle j|\psi_{k+q}^{\alpha_2}\rangle\langle\psi_{k+q}^{\alpha_2}|i\rangle}{\epsilon_{k+q}^{\alpha_2} - \epsilon_k^{\alpha_1} - (\omega + i\eta)}(n_F(\epsilon_{k+q}^{\alpha_2}) - n_F(\epsilon_k^{\alpha_1})). \tag{S6}$$

Here, i, j denotes the orbital degrees of freedom and α_i the band index. The static limit is derived by setting $\omega = 0$ and a small numerical η value.

To analyze the static susceptibility matrix, we can focus on the total response by summing over states i and j. When taking the limit $q \to 0$, the susceptibility would approach the limit $\chi_0^0 \to 2\mu_B^2\rho(E_f)$ with the density of states smeared by temperature β^{-1} at the Fermi level E_f. On the other hand, one could consider the mode decomposition of the response matrix $\bar{\chi}_{ij}^0 = \chi_{ijij}^0$ and sort the eigen modes by their eigenvalues ϵ_n, from $\bar{\chi}_{ij}^0 e_n = \epsilon_n e_n$. This analysis allows us to extract the dominant response mode in the susceptibility. In Fig. S7(a,b), we computed the susceptibility mode decomposition along the high-symmetry line (a) and on the $q_z = 0$ plane (b), respectively. This can be contrasted with the conventional ferromagnetic state where the response is dominated at the Γ point. Here the response is dominated on the $q_z = 0$ plane with maximum values around the BZ boundary.

Another quantity of interest is the static local susceptibility $\chi_{\rm loc}^0$ defined as

$$\chi_{\rm loc}^0(\omega = 0) = -\frac{2\mu_{\rm B}^2}{\beta} \sum_{ij} \sum_{i\omega_n} G_{ij}^{0,\rm loc}(i\omega_n) G_{ji}^{0,\rm loc}(i\omega_n), \tag{S7}$$

where the local Green's function $G_{ij}^{0,\rm loc}$ is

$$G_{ij}^{0,\rm loc}(i\omega_n) = \frac{1}{N_{\vec{k}}} \sum_{\vec{k}} G_{ij}^0(\vec{k}, i\omega_n). \tag{S8}$$

We compute $\chi_{\rm loc}^0$ for the effective model and the result is shown in Fig. S7(c) (we note that $\chi_{\vec{q}=0}^0$ is of a similar magnitude and shows a similar temperature evolution). In contrast to metallic systems in the limit of weak correlation whose $\chi_{\rm loc}^0$ is expected to be temperature-independent [S7], the enhancement of $\chi_{\rm loc}^0$ with decreasing temperature suggests the pre-formation of local moments. Fitting the high-temperature part with $\chi_{\rm loc}(T) = \frac{\mu^2}{3(T+2T_K)}$ gives $\mu = 0.95\mu_B$ and $T_K = 440$ K. Since correlation effects are severely underestimated in DFT, we expect that in our procedure the Kondo temperature T_K is strongly overestimated [S8]. In Fig. S7(d) we compare the calculated $\chi_{\rm loc}$ with the experimentally measured χ_c; the latter appears approximately two orders of magnitude larger, implying that correlation effects

need to be considered to achieve a quantitative understanding of the experimental magnetic susceptibility of Ni_3In. For instance, more advanced interacting theories are needed to account for the vertex corrections beyond correlations at the one-particle level. Nevertheless, this model suggests that the flat band of Ni_3In supports the formation of local moments even in the absence of explicit correlation effects [S8]. The relative flatness of the response within the in-plane momentum near $q_z = 0$ (Fig. S7(a,b)) points towards an interaction beyond simple itinerant magnetism where well-defined momentum space hot spots are believed to be the driving force of magnetic order, whereas a flat momentum-dependence of $\chi(\boldsymbol{q})$ is associated with local moment-based magnetic fluctuations [S9]. The fundamental nature of the magnetic instability of the system is the subject of ongoing investigation.

SIV. ARPES of Ni_3In

To identify the high-symmetry points along the k_z momentum-space direction, we obtained photon energy-dependent ARPES spectra over a wide energy range from 70 eV to 230 eV. The corresponding k_z is calculated by assuming the nearly-free-electron final state with inner potential 10 eV. The energy range investigated here covers more than two full Brillouin zones of Ni_3In as shown in Fig. S8 (a,b).

The $k_z = 0 \pmod{2\pi/c}$ planes could be identified near two photon energies, 124 eV (corresponds to $k_z = 5.93$ Å^{-1} or $8\pi/c$) and 200 eV (corresponds to $k_z = 7.41$ Å^{-1} or 10π). It is noteworthy that the spectra at $k_z = 8\pi/c$ and $k_z = 10\pi/c$ exhibit very different matrix elements as contrasted in Fig. S8(c,d) (both agree with part of the predicted band dispersions scaled with a factor of 80% shown as green lines). For example, the spectrum obtained at $k_z = 10\pi/c$ (Fig. S8(d)) displays a prominent electron pocket at Γ and intense hole-like bands at M, while these features are absent in the spectrum obtained at $k_z = 8\pi/c$ (Fig. S8(c)), despite the fact that they represent same momentum-planes in the Brillouin zone. We attribute this strong matrix element effect to the bilayer kagome structure in the unit cell of Ni_3In: the photo-electrons from two kagome layers in the unit cell may interfere differently at $k_z = 8\pi/c$ and $k_z = 10\pi/c$ resulting in the doubling of apparent periodicity observed in Fig. S8(a,b) from the real periodicity of the Brillouin zone in Ni_3In.

In Fig. S8(d) at $k_z = 8\pi/c$, we observe a clear crossing between the electron-like and hole-like bands near the zone center Γ. As shown in the Fermi surface of Fig. S8(e), the

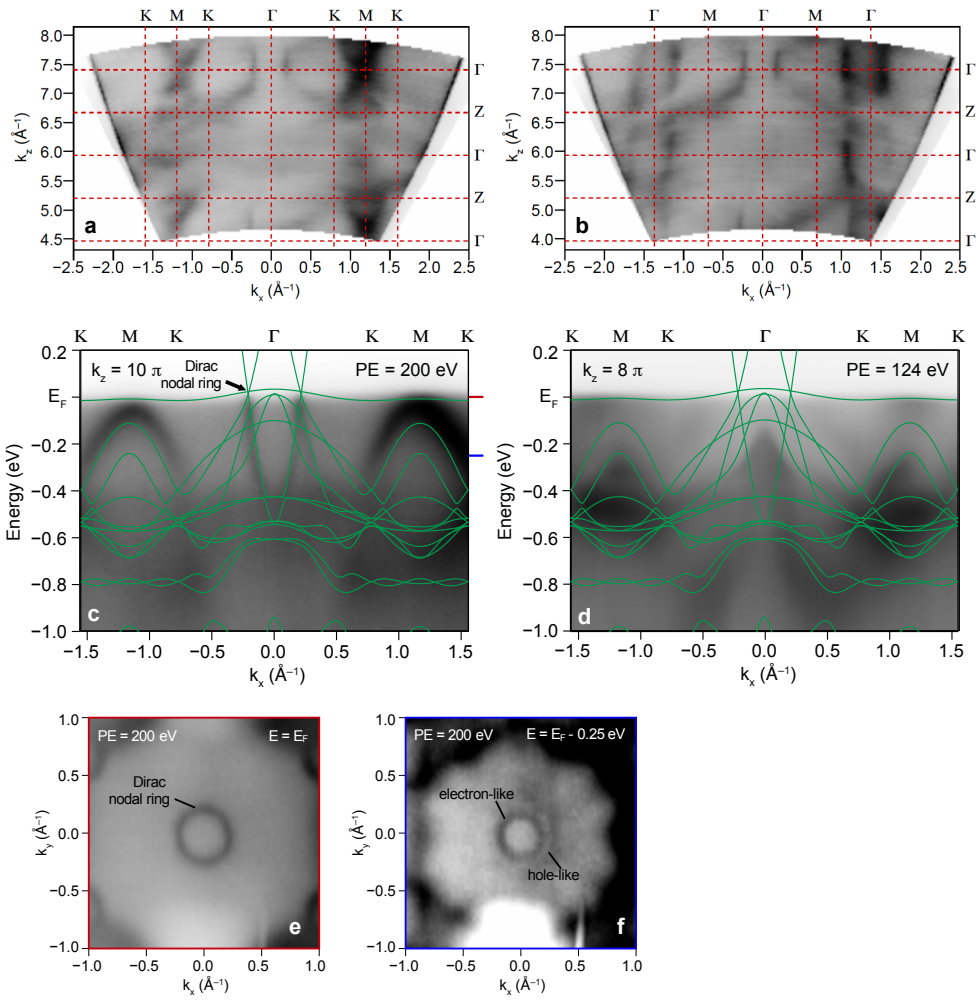

FIG. S8. **Photon-energy dependent ARPES and the Dirac nodal ring in Ni_3In** (a,b) $k_x - k_z$ cut at E_F along $\mathrm{K}-\mathrm{M}-\mathrm{K}-\Gamma$ (a) and along $\mathrm{M}-\Gamma$ (b), respectively. (c,d) The measured band structure along $\Gamma-\mathrm{K}-\mathrm{M}$ directions at $k_z = 8\pi/c$ (c) and $k_z = 10\pi/c$ (d) overlaid with the overall DFT band structure renormalized by 80% (green lines). (e,f) Constant energy maps at $E = E_F$ (e) and $E = E_F - 0.25$ eV (f) at $k_z = 10\pi/c$. The energy positions of (e) and (f) are denoted in (c) by red and blue markers, respectively.

crossing between electron- and hole-like bands gives rise to the Dirac nodal ring at E_F as predicted by the density functional theory calculations (see Fig. 1(e) and Fig. S3 for example). At E_F (Fig. S5(e)) we observe the Fermi wave vector $k_F = (0.21 \pm 0.02)\,\text{Å}^{-1}$ along $\Gamma-\mathrm{K}$ and $k_F = (0.23 \pm 0.03)\,\text{Å}^{-1}$ along $\Gamma-\mathrm{M}$ directions, respectively, consistent with the DFT nodal ring wave vector k_{NR} given above. We estimate the Fermi velocity of the electron-like dispersion of the nodal ring as $(11.2 \pm 1.4) \times 10^5\,\mathrm{m}\cdot\mathrm{s}^{-1}$ and the hole-dispersion

to be $(-5.1 \pm 0.4) \times 10^5\,\mathrm{m \cdot s^{-1}}$. Away from E_F, the degeneracy of the nodal ring is lifted in k-space, and two split pockets (small electron- and large hole-pockets) can be observed in the constant energy contour at $E = E_F - 0.25$ eV as displayed in Fig. S8(f).

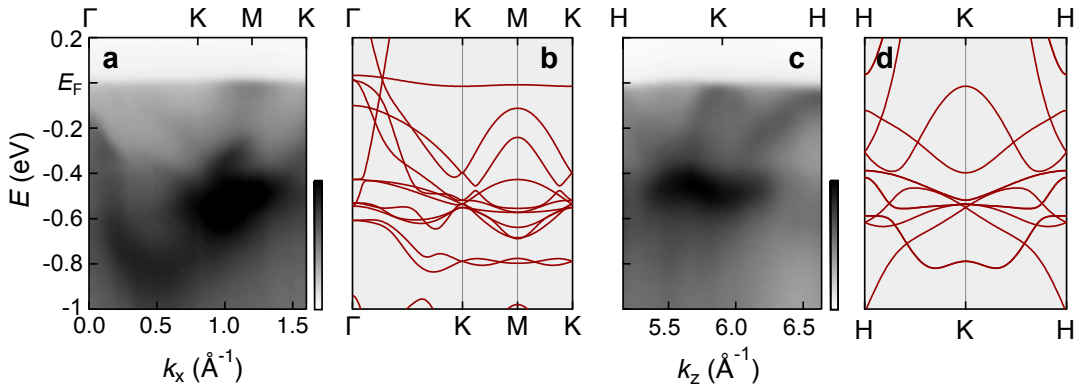

FIG. S9. **Angle-resolved photoemission spectroscopy (ARPES) of Ni_3In** (a-d) ARPES spectra measured at 20 K of Ni_3In (a,c) contrasted with corresponding DFT band structure (b,d). (a,b) are along an in-plane $\Gamma - \mathrm{K} - \mathrm{M} - \Gamma$ momentum cut and (c,d) are along an out-of-plane $\mathrm{H} - \mathrm{K} - \mathrm{H}$ momentum cut. The DFT band dispersions in (b,d) are renormalized by a factor of 0.8.

In Fig. S9 we focus on the flat band states of Ni_3In in ARPES: in Fig. S9(a) in the $\Gamma - \mathrm{K} - \mathrm{M} - \Gamma$ plane, ARPES intensity at E_F can be found near M; additionally, since the in-plane flat band is expected to disperse along $\mathrm{H} - \mathrm{K} - \mathrm{H}$, that the band top touches E_F at K (Fig. S9(c)) is consistent with the expectation that the in-plane dispersion of the same band is at E_F. By renormalizing the DFT bands by a factor of 0.8, we find reasonable agreement with the overall dispersive features from ARPES, suggesting that the flat band placed at E_F by DFT sets an adequate starting point for the understanding of the unusual transport and thermodynamic responses observed in Ni_3In.

In Fig. S10 we performed second derivative analysis of the ARPES intensities and overlay them with the DFT dispersions with 80% renormalization. Derivatives are taken along the energy and momentum directions for Fig. S10(a) and Fig. S10(b,c), respectively. In Fig. S10(a) near E_F there is intensity originating from the Fermi-Dirac distribution with an enhancement near K and M. Additionally, the intensity at E_F near K can be seen to strongly disperse downward in Fig. S10(c). These observations capture the key predicted characteristics of the flat band in Ni_3In: (I) in the $k_z = 0$ plane the flat band is depleted near Γ while occupied near M and K; (II) along k_z the same band disperses down in energy and

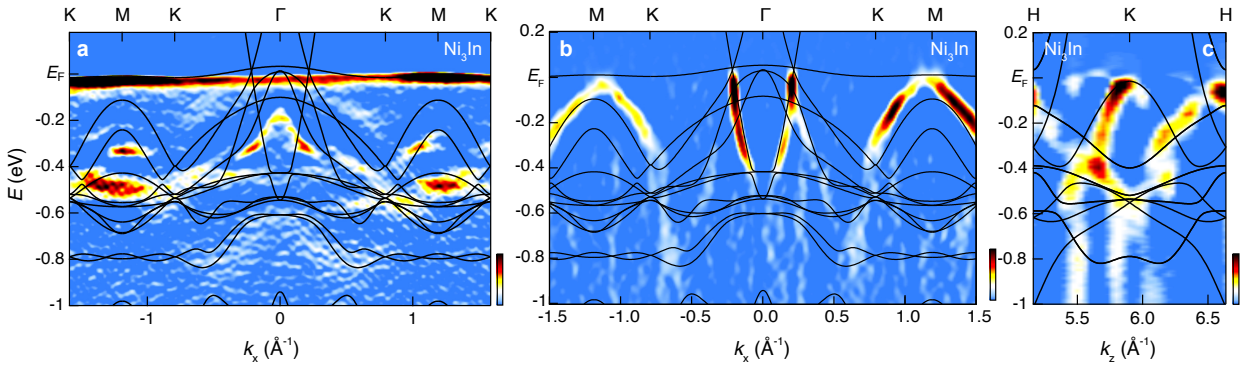

FIG. S10. **Second derivatives of Ni_3In ARPES spectra overlaid with DFT bands** (a) Second-derivative (energy) of ARPES intensity in the $k_z = 10\pi/c$ plane. (b) Second-derivative (momentum) of ARPES intensity in the $k_z = 8\pi/c$ plane. (c) Second-derivative (momentum) along the H-K-H direction. Black solid lines in (a-c) depict DFT dispersion and are scaled by a factor of 80%. The raw data to which we apply the derivative analysis to generate (a-c) can be found in Fig. S8(c), (d), respectively.

its band maxima is at the $k_z = 0$ plane. In Fig. S10(b) we show the momentum (k_x) second-derivative of ARPES intensity at the $k_z = 8\pi/c$ plane, which captures the predicted non-flat-band features in DFT at $k_z = 0$–the agreement between DFT and ARPES is apparent for both the highly dispersive Dirac nodal ring feature enclosing Γ and the downward-bending quadratic dispersion near M.

Comparing the ARPES spectra of Ni_3In with that of the isostructural compound Ni_3Sn provides an additional view of the flat band. We first contrast the DFT electronic structures of Ni_3In with that of Ni_3Sn in Fig. S11. The characteristic band features including a flat band in the $k_z = 0$ plane and a crossing near K are similar in both compounds with an overall upward shift of E_F in Ni_3Sn by approximately 0.2 eV with respect to the flat band. This suggests that we can utilize the electron filling of Ni_3Sn to better spectroscopically investigate the flat band present across this class of nickel-based binary kagome metals.

In Fig. S12 we show the ARPES spectra obtained from single crystals of Ni_3Sn; we contrast in particular the k_z-dispersion of Ni_3Sn and Ni_3In. In both Ni_3In and Ni_3Sn we observe a quadratic, downward-bending dispersion whose maximum locates near K (highlighted by the arrows in Fig. S12(a,b)). In Ni_3Sn since the in-plane dispersion is fully below E_F, we observe a flat dispersion with bandwidth $\sim$ 60 meV within the in-plane momentum cut

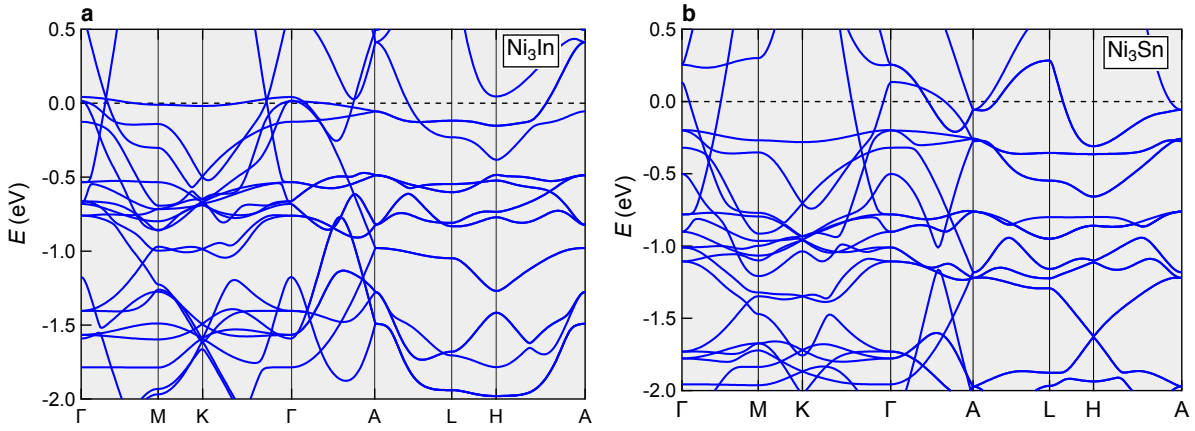

FIG. S11. **Electronic structure of Ni_3In and Ni_3Sn** Calculated electronic structure of Ni_3In (a) in comparison with Ni_3Sn (b). Ni_3In exhibits a flat band in the $\Gamma - M - K - \Gamma$ at E_F while in Ni_3Sn a similar flat band is near -0.2 eV.

in Fig. S12(c) (highlighted by a blue arrow). To better visualize these bands, we further took the second derivatives of Fig. S12(a,b) (momentum) and Fig. S12(c) (energy) and the resulting spectra are overlaid with DFT with 80% renormalization in Fig. S12(d-f). That the band-top-intensity near K in Ni_3Sn (Fig. S12(b,e)) is moved to E_F in Ni_3In (Fig. S12(a,d)) suggests a rigid band shift picture; although a complete resolution of the in-plane flat dispersion is smeared by the Fermi-Dirac distribution in Ni_3In, the observation of the flat dispersion across the entire in-plane momenta in Ni_3Sn (Fig. S12(c,f)) provides strong evidence of the flat band. We note that moderate intensities at E_F in Fig. S12(f) arise from taking the second order energy derivative of the Fermi-Dirac distribution.

SV. Magnetotransport responses of Ni_3In

The magnetoresistance (MR) response $\Delta\rho_{ab} \equiv \rho_{ab}(H) - \rho_{ab}(H = 0)$ is shown in Fig. S13(a). The dominant response is a negative MR that grows rapidly with decreasing T, which we ascribe to field-induced suppression of magnetic fluctuations akin to that observed in magnetic metals above their ordering temperatures [S10]. At the lowest T and highest H a positive curvature appears. The positive MR is found to be stronger with fields in the ab-plane than along the c-axis in field rotation measurements, consistent with the steep band dispersion perpendicular to the kagome planes. Limiting our discussions to the low H- and

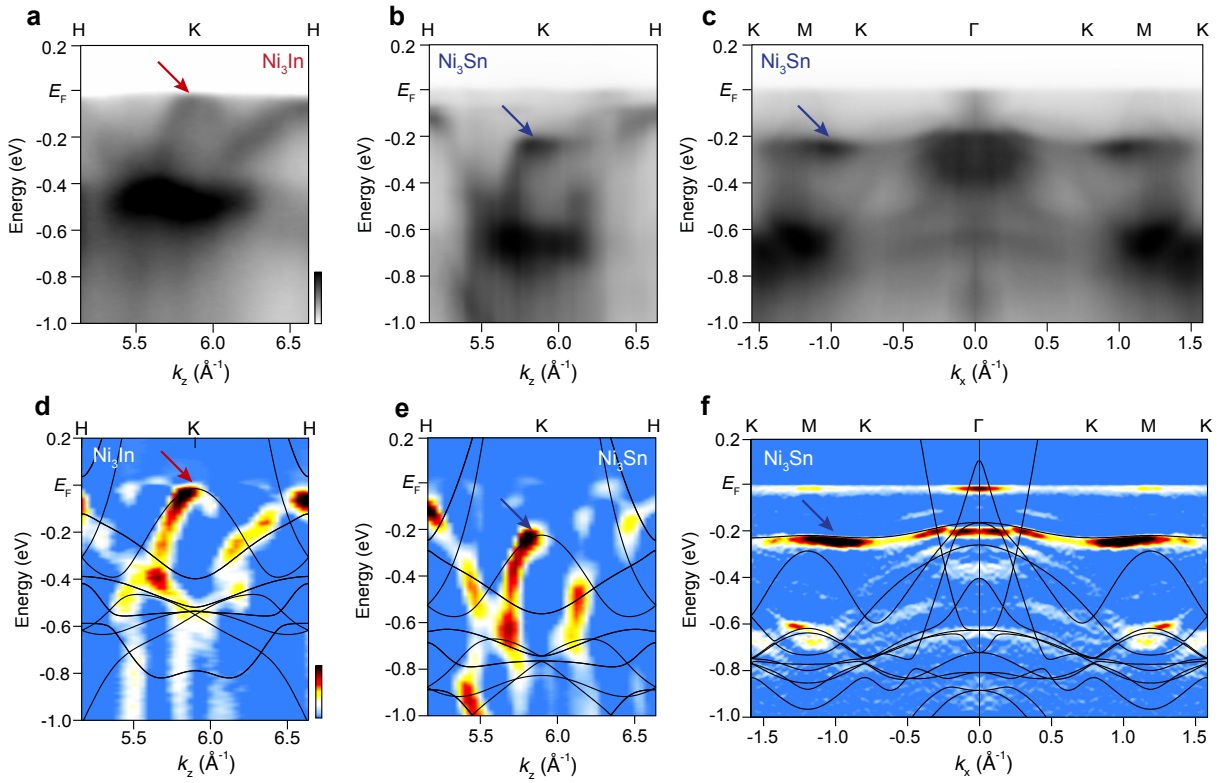

FIG. S12. **ARPES of Ni_3Sn** (a,b) H − K − H cut of ARPES intensity in Ni_3In (a) and Ni_3Sn (b); (c) shows the ARPES intensity of Ni_3Sn in the $k_z = 0$ plane along K − M − K − Γ − K − M − K. (d,e) Momentum second-derivative of (a) and (b), respectively. (f) Energy second-derivative of (c). The arrows in (a-f) highlight the photoemission signatures that are associated with the flat band. Solid black lines in (d-f) are the DFT bands of Ni_3In (d) and Ni_3Sn (e-f) renormalized with a scaling factor of 0.8.

elevated T- regime where negative MR is observed, we find the MR can be scaled against $\mu_0 H/(T + T^*)$ with $T^* = 8.5$ K (see Fig. S13(b) and (c)). This form of scaling was first applied to the experimental data of heavy fermion compound UBe_{13} with T^* comparable with the Kondo temperature characterizing the antiferromagnetically coupled local moments and conduction electrons [S11], suggesting a local moment component of the fluctuating magnetism in Ni_3In.

In particular, we followed the $J = 1/2$ Bethe-ansatz solution of the Kondo model [S12] to capture the negative component of the MR in Ni_3In. The MR in Kondo systems originates from the lifting of the local moment degeneracy by the magnetic field, which in turn reduces the strength of Kondo resonance responsible for scattering of the conduction electrons

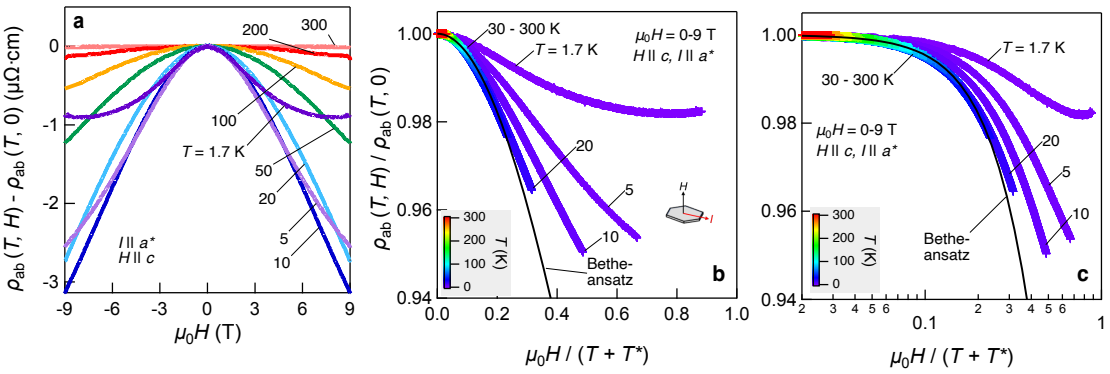

FIG. S13. **Negative Magnetoresistance and its scaling based on the Bethe-ansatz solution of the Kondo model** (a) In plane MR $\Delta\rho_{ab} = \rho_{ab}(T,H) - \rho_{ab}(T,0)$ as a function of magnetic field $\mu_0 H$ at selected T. (b,c) $\rho_{ab}(T,H)/\rho_{ab}(T,0)$ scaled against the renormalized magnetic field $\mu_0 H/(T+T^*)$ displayed in the linear (b) and logarithmic scale (c). In (b,c) each color represents data taken at a constant temperature (color scale shown in the legend). Inset in (b) shows the measurement configurations. The black solid line in each panel represents a fit to Eq. (S9).

[S13]. The functional form has been given quantitatively in the Bethe-ansatz solution of the Coqblin-Schrieffer (Kondo) model in the ground state by Schlottmann [S12] (black solid curve in Fig. S13(b) and (c)) as:

$$\rho(H)/\rho(0) = \frac{2}{\sin^{-2}(\pi n_+) + \sin^{-2}(\pi n_-)}. \tag{S9}$$

Here n_+ and n_- are the occupation numbers of spin up and spin down local moments, respectively. $n_\pm$ may be obtained via $n_\pm = \frac{1}{2} \pm m_i$ where the impurity magnetization per site m_i

$$m_i = \frac{1}{4} + \frac{i}{4\pi^{3/2}} \int_{-\infty}^{+\infty} \frac{dy}{y} \Gamma(\frac{1}{2} + i\frac{y}{2}) \cdot e^{-iy\ln(H/H^*)} (-iy+0)^{-i\frac{y}{2}}. \tag{S10}$$

Here H^* is a characteristic energy scale of the Kondo coupling. At finite T, H^* is empirically found to grow in proportion to $k_B T$, where $H^* = \frac{k_B(T+T^*)}{g\mu_{\rm eff}\mu_0}$, and T^* plays the role of the Kondo temperature [S11]. We show the MR of ρ_{ab} with $\mu_0 H/(T+T^*)$ in linear and logarithmic scales, respectively, in Fig. S13(b,c) with $T^* = 8.5$ K. Eq. (S9) reasonably describes the behavior above 20 K, with a deviation seen when the positive MR (described above) sets in below $T = 20$ K. From this we find that $g = 3.9$ if we assume that for each Ni atom $\mu_{\rm eff} = 1\mu_B$ as inferred from the magnetic susceptibility measurements (χ_c). Alternatively, if we assume that for each triangular plaquette $\mu_{\rm eff} = 1.77\mu_B$ (deduced from

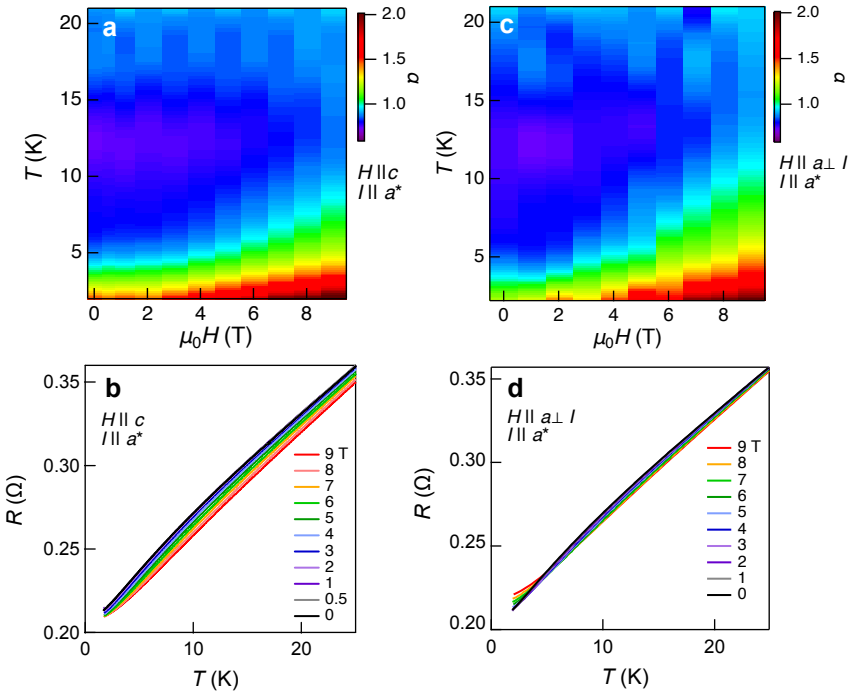

FIG. S14. (a-d) Resistivity power law in two different current/field orientations for the ab plane response measured on a FIB sample. (a,c) show $\alpha(H,T)$ and (b,d) show the corresponding $R(T)$ from which α is extracted via $\alpha \equiv \partial \ln(R(T) - R_0)/\partial \ln T$ where R_0 is an extrapolated zero temperature limit.

χ_c), we then find $g = 2.3$.

Examining the evolution of the temperature-exponent α in $\rho(T) \sim T^{\alpha}$ at fixed H provides additional perspective on the nature of conduction electrons near the Fermi surface in Ni_3In in the context of the observed non-Fermi liquid behavior (such analysis has been applied to a series of field-tuned non-Fermi liquid systems [S14]). In Fig. S14(a) and (c) we contrast $\alpha(H,T)$ obtained from $H \parallel c, I \parallel a^*$, and $H \parallel ab, H \perp I$. The evolution of α with temperature and magnetic fields are little affected by the configuration: in both Fig. S14(a,c), magnetic field acts to bring the system closer to a Fermi liquid state ($\alpha \to 2$) as we schematically illustrate in main text Fig. 4(a)–this is consistent with an isotropic coupling between the applied magnetic field and underlying quantum fluctuations likely of magnetic nature.

In Fig. S15 we summarize the low temperature transport of ρ_{ab} of Ni_3In at selected magnetic fields. The presence of a low temperature Fermi liquid regime where $\rho(T) =$

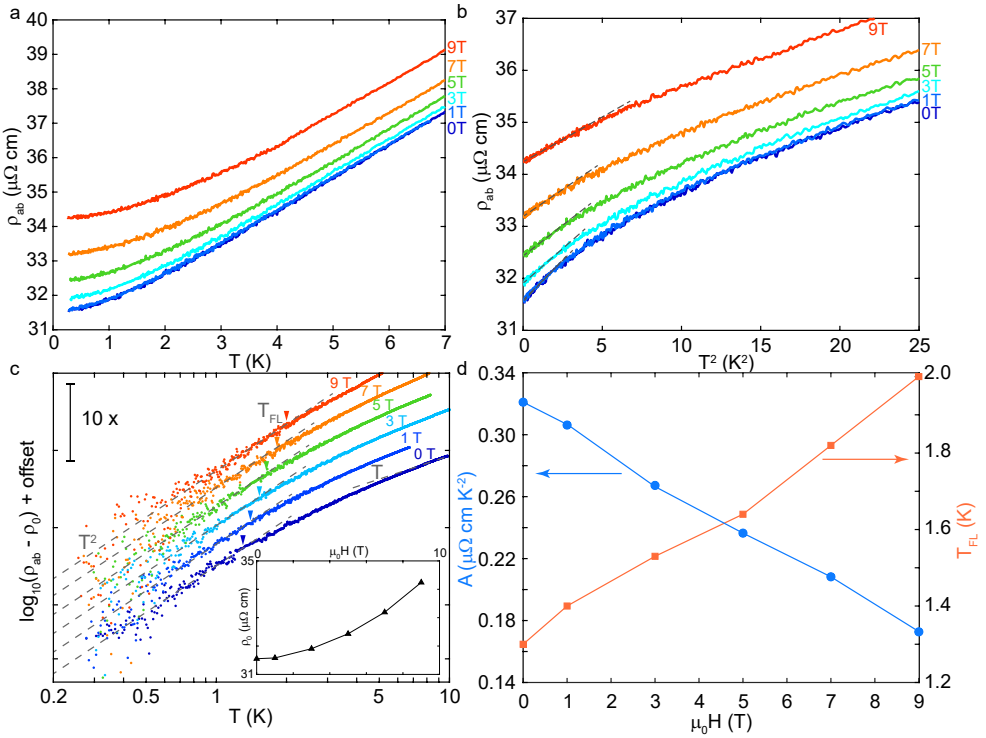

FIG. S15. **Low temperature transport of Ni_3In** (a,b) $\rho(T)$ plotted with T (a) and T^2 (b) at selected magnetic fields applied out of the kagome plane, respectively. (c) $\rho - \rho_0$ with respect to T in a log-log plot. Data taken at different magnetic fields are offset for clarity. The inset shows the estimated ρ_0 at each field. (d) Left axis: A coefficient at different magnetic fields for Ni_3In obtained from fitting below 1.25 K; right axis: T_{FL} at each field below which $\rho(T) \sim \rho_0 + AT^2$.

$\rho_0 + AT^2$ holds is most clearly seen in Fig. S15(b) when ρ is plotted against T^2 and in Fig. S15(c) where $\rho - \rho_0$ is shown against T in a log-log plot: the coefficient A (slope of dashed lines in Fig. S15(b)) decreases with applied H while the temperature regime below which T^2 is observed increases with H. These trends are further summarized in Fig. S15(d). Both the considerable decrease of A with H and the increase of T_{FL} with H are consistent with magnetic field suppression of underlying quantum fluctuations of magnetic nature and the system being driven away from a potential quantum critical point.

SVI. Additional transport data and modified Kadowakoi-Woods ratio

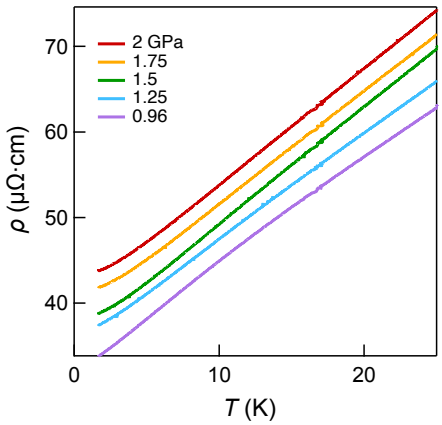

FIG. S16. **At-pressure resistivity of Ni_3In** At-pressure in-plane $\rho(T)$ of Ni_3In between 2 to 25 K, from which we extract the $\alpha(P,T)$ displayed in main text Fig. 3c. The curves taken under different pressures are offset for clarity.

$\rho(T)$ curves used to extract the at-pressure resistivity exponents are shown in Fig. S16. The pressure-induced "flattening out" of the curves at the low temperature end is apparent in the curves, which corresponds to enhanced α in the lower right corner of the $P-T$ phase diagram displayed in main text Fig. 3c.

In Fig. S17a we show the ab plane normalized resistivity $\rho/\rho_{300\,\mathrm{K}}(T)$ for three different samples, and the main features in the $\rho(T)$ curves, including the roll-over around 100∼150K, and near-linear-T behavior below 100 K are reproduced in all these measurements. In Fig. S17(b,c) we discuss the c-axis resistivity ρ_c of Ni_3In. The overall value of ρ_c is lower than that of ρ_{ab}, and crucially it also shows a strong deviation from a prototypical Fermi liquid behavior: a test fit to T^α of ρ_c between 1.7 to 10 K yields $\alpha = 1.198 \pm 0.003$ (dashed line in Fig. S17c). Thus, in our experiments both ab-plane and c-axis transport exhibit strong deviation from the conventional FL behavior (observed in many of the other kagome metals, see e.g. Fig. S19).

In addition to the Kadowaki-Woods plot shown in main text Fig. 2(c), we also compare Ni_3In with other systems in the context of the modified Kadowaki-Woods ratio discussed in Ref. [S16]. Using DFT values of carrier density ($n_{tot} = \sum |n_i|$, where we sum over all bands at the Fermi level) $n_{tot} = 7.29 \times 10^{27}\mathrm{m}^{-3}$, bare density of states $D_0 = 1.19 \times$

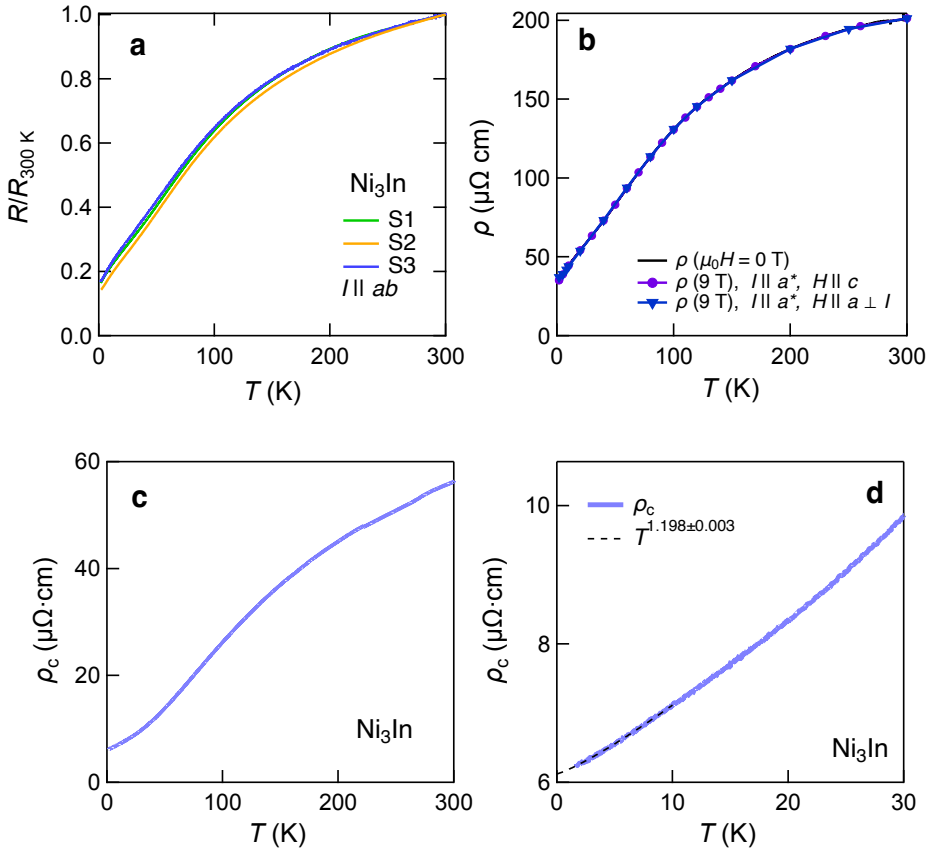

FIG. S17. (a) Normalized in-plane resistivity $\rho/\rho_{300\ \mathrm{K}}$ as a function of T in three different samples of Ni_3In. (b) $\rho(T)$ over 1.7-300K at 0 T (black curve) and 9 T(purple and blue symbols, the respective current/field configurations are noted in the legends). (c,d) Resistivity along the c-axis ρ_c of Ni_3In shown from 1.7-300 K (c) and 1.7 to 30 K (d). Dashed line in (d) indicate a fit of ρ_c between 1.7 to 10 K to $\rho_0 + AT^{\alpha}$, and the obtained exponent is $\alpha = 1.198 \pm 0.003$.

$10^{48}\mathrm{m}^{-3}\mathrm{J}^{-1}$, average Fermi velocity in the ab plane $5.67{\times}10^4$ m/s, and the experimental value of volumic Sommerfeld coefficient 1.64×10^3 J $\mathrm{K}^{-1}\mathrm{m}^{-3}$ we obtain $\gamma^2/fdx(n) = 8.16 \times 10^{-128}$ $\mathrm{kg}^4\mathrm{m}^9\mathrm{s}^{-6}\mathrm{K}^{-4}$. This puts Ni_3In close to the modified Kadowaki-Woods scaling discussed in Ref. [S16] and suggests that the reduced Fermi velocity of the flat electronic dispersions near E_F plays a key role in the large Kadowaki-Woods ratio of the system.

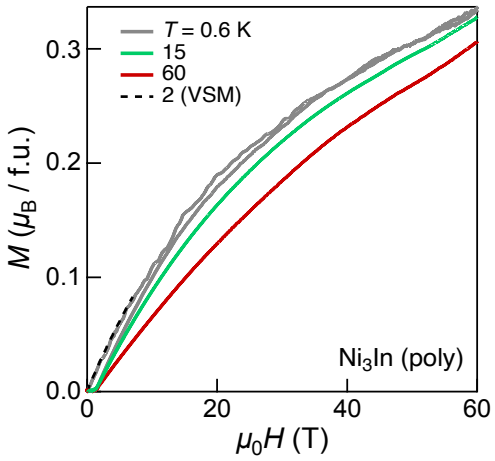

FIG. S18. **Pulsed field magnetization of Ni_3In** Pulsed field magnetization of polycrystalline Ni_3In at selected T (solid curves). Dashed line indicates low field $M(H)$ of polycrstalline Ni_3In obtained from in-house VSM measurements.

SVII. High field magnetization

We have performed pulsed field magnetization measurements up to 60 T on polycrystalline samples of Ni_3In; the results are shown in Fig. S18 where no field-induced magnetic ordering is observed. This is consistent with the observed $\alpha(T, H)$ shown in main text Fig. 3b and proposed phase diagram in main text Fig. 4a that magnetic field appears to promote a Fermi liquid state from the non-Fermi liquid state near zero field, and likely away from a potentially nearby ordered state.

SVIII. Metallic character of binary kagome metals

We show in Fig. S19 the resistivity as a function of T for different single crystals in the binary kagome metal family. These include ferromagnetic Fe_3Sn and Fe_3Ge, antiferromagnetic FeSn, Pauli paramagnets Ni_3Sn and CoSn, and the presently studied Ni_3In. Aside from Ni_3In, the resistivities of these kagome metals saturate at low temperature, showing typical Fermi liquid metallic behavior regardless of the underlying magnetic order. Ni_3In stands out in this way in showing non-Fermi liquid behavior and also that among these materials it is the only which has a flat band at E_F. We note that at $T < 1$ K, the resistivity of Ni_3In tends to saturate to a Fermi-liquid like behavior as shown in Fig. S19(f) inset. One

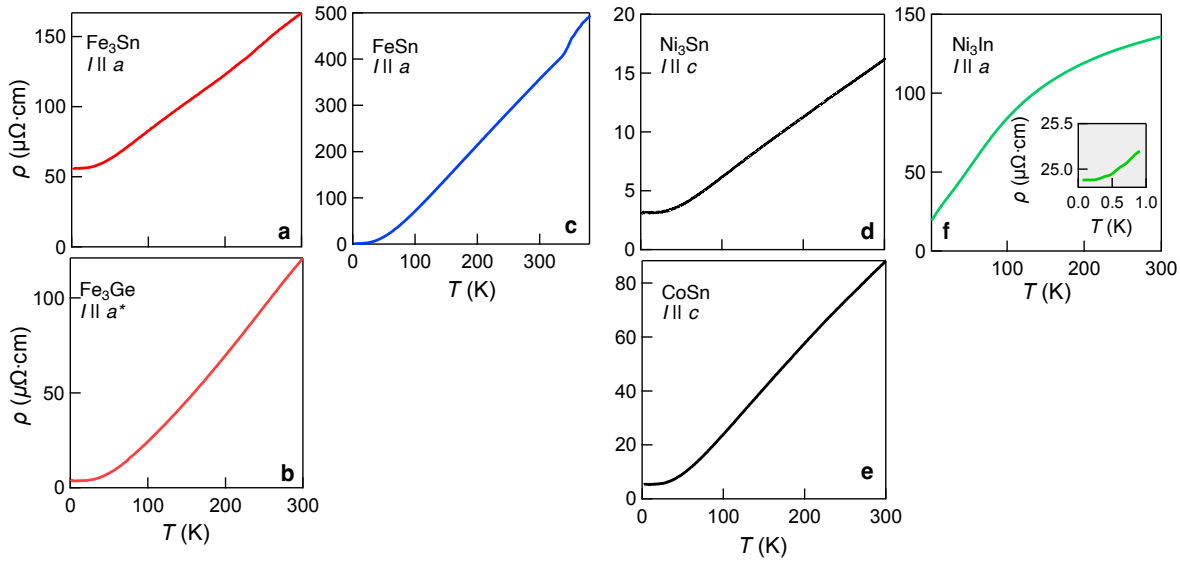

FIG. S19. **Temperature evolution of resistivity in binary kagome lattice single crystals** (a) Fe_3Sn, (b) Fe_3Ge, (c) FeSn, (d) Ni_3Sn, (e) CoSn and (f) Ni_3In. The inset of (f) shows the resistivity of Ni_3In below 1 K.

possibility is that further fine tuning may be required to achieve the quantum critical point at the milli-Kelvin temperature scale. We obtain a quadratic coefficient $A = 0.5\,\mu\Omega\cdot\mathrm{cm}\cdot\mathrm{K}^{-2}$ ($\rho(T) = \rho_0 + AT^2$).

SIX. Heat capacity of Ni_3In

In Fig. S20(a) we compare the overall C_p/T to that predicted by the Debye model (Eq.S11) [S15]:

$$C_p(T) = 9Nk_B(\frac{T}{T_D})^3 \int_0^{T_D/T} \frac{y^4 e^y}{(e^y-1)^2} dy + \gamma T. \tag{S11}$$

Here N is the number of atoms, k_B is the Boltzmann constant, γ the Sommerfeld coefficient and T_D is the Debye temperature characterizing the energy scale of phonons in the system. The experimental C_p/T compares reasonably well with the prediction of the Debye model with $T_D = 327$ K. The associated resistivity induced by phonon scattering (Eq.S12) is given by the Bloch-Grüneisen model [S15]:

$$\rho_{\mathrm{cal}}(T) = \rho_{ph}(\frac{T}{T_D})^5 \int_0^{T_D/T} \frac{y^5 e^y}{(e^y-1)^2} dy. \tag{S12}$$

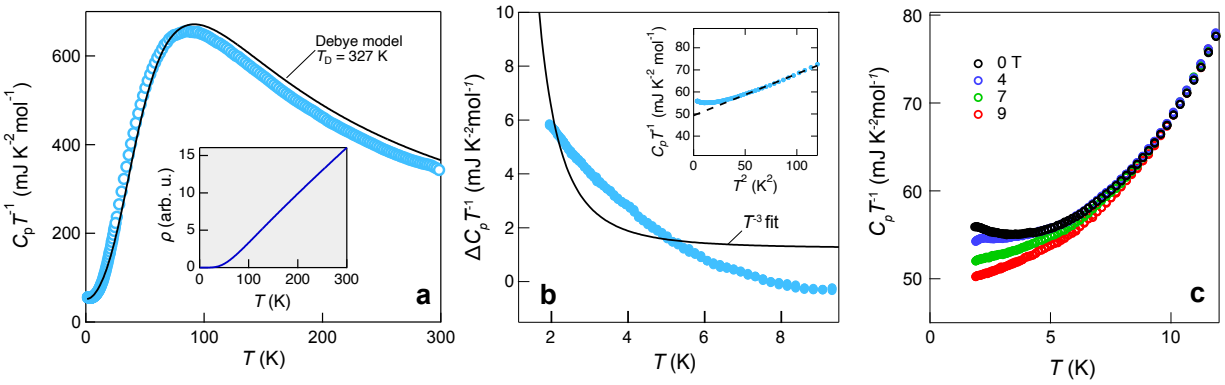

FIG. S20. **Heat capacity of Ni_3In** (a) C_p/T over a wide T range (circles) as compared to the Debye model with $T_D = 327$ K together with a Sommerfeld term with $\gamma = 51.6$ mJ·K^{-2}·mol^{-1} (black solid line). The inset shows the expected resistivity $\rho_{\rm cal}$ calculated from phonon scattering (see supplementary text). (b) Fit of $\Delta C_p/T \equiv C_p/T - \beta T^2 - \gamma$ to T^{-3}. The dashed line in inset indicates $\beta T^2 + \gamma$. (c) C_p/T with respect to T at selected magnetic fields.

Here ρ_{ph} is a material dependent parameter proportional to the electron-phonon coupling. The resistivity $\rho_{\rm cal}(T)$ associated with the above Debye model is shown in Fig. S20(a) inset. This trend and the temperature range of phonon-induced T-linear resistivity qualitatively resembles the $\rho(T)$ of the non-magnetic and magnetically ordered kagome metals as shown above, suggesting that these materials are sufficiently distant from quantum criticality and that phonon scattering dominates $\rho(T)$ at elevated T. Also, it suggests that T_D of these cousin kagome metal materials are comparable, perhaps unsurprising given their similar structural and elemental composition. The qualitative difference between $\rho(T)$ of Ni_3In and $\rho_{\rm cal}$ implies that conventional phonon scattering cannot account for the peculiar ρ observed therein.

We also briefly discuss potential contribution to the heat capacity from a nuclear Schottky anomaly. That the low T-rise in C_p cannot be fit with T^{-2} (Fig. S20(b)), and that magnetic fields tend to suppress C_p instead of increasing C_p (Fig. S20(c)) contradicts a nuclear Schottky scenario [S17]. Instead we attribute the low T-rise in C_p/T to an electronic non-Fermi liquid origin; that a Fermi-liquid-like behavior is partially recovered at 9 T in C_p/T (main text Fig. 3a) is also consistent with our proposed tendency of field-induced Fermi liquid phase from transport.

SX. Magnetic susceptibility of Ni_3In

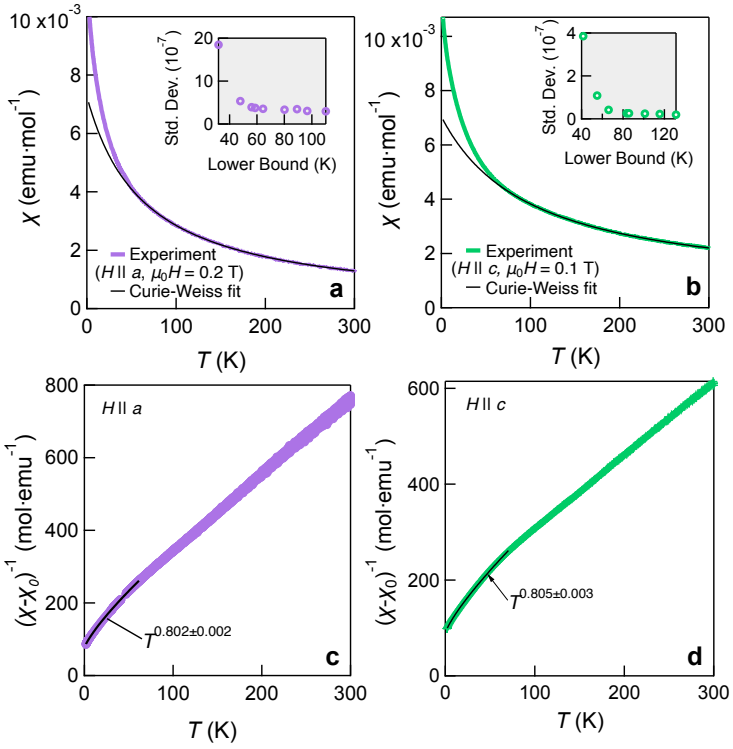

FIG. S21. **Magnetic susceptibilities of single crystalline Ni_3In** (a) In-plane magnetic susceptibility χ (purple line) measured with an applied field of 0.2 T. The solid black line represents a Curie-Weiss fit from 60 to 300 K. (b) Out-of-plane χ (green line) measured at 0.1 T. The solid black line represents a Curie-Weiss fit from 86 to 300 K. The insets of (a) and (b) show the fitting range dependence of the quality of the respective fits. We note that we have checked the linearity of M with H up to 0.2 T. (c,d) The black curve depicts a fit of χ along a (c) and c (d) below 60 K to a modified Curie-Weiss law $\chi^{-1} = A + BT^{\alpha}$.

We summarize the magnetic properties of single crystalline Ni_3In in Fig. S21, where in (a,b) we highlight a rise of the magnetic susceptibility χ with decreasing temperature T under both in and out-of-plane H. The high T part of both χ_a and χ_c can be fit with a Curie-Weiss form (black solid lines in Fig. S21(a,b)):

$$\chi = \chi_0 + \frac{C}{T - \theta}, \tag{S13}$$

with χ_0 as the temperature-independent part of χ, C the Curie constant, θ the mean-field Curie-Weiss temperature. We note that both χ_a and χ_c at low T deviate from a Curie-

Weiss behavior as can be seen from the rapid rise of the standard deviation of the fit below approximately 60 K and 80 K for χ_a and χ_c, respectively (Fig. S21(a,b) insets). The solid lines we show in Fig. S21(a,b) yield $\theta_a = -64.2 \pm 0.2$ K and $\theta_c = -100.9 \pm 0.6$ K. The effective magnetic moments inferred from $C = \dfrac{\mu_0 N}{3k_B}\mu_{\text{eff}}^2$ (μ_{eff} is the effective magnetic moment) are $1.1\mu_B$ and $1.3\mu_B$ per Ni for $H \parallel a$ and $H \parallel c$.

We find that at low temperature (below ~ 70 K) we may describe both $\chi_a(T)$ and $\chi_c(T)$ of Ni_3In with a modified Curie-Weiss law in which T is replaced by a more generalized form T^α, which has been discussed as a signature of non-Fermi liquid metals [S18, S19]:

$$(\chi - \chi_0)^{-1} = A + BT^\alpha. \tag{S14}$$

The extracted α from the fitting shown in Fig. S21(c) is $\alpha_a = 0.802 \pm 0.002$, and in (d) $\alpha_c = 0.805 \pm 0.003$. Theoretically a modified Curie-Weiss law with $\alpha < 1$ has been discussed in the context of quantum criticality associated with localization of magnetic moments in heavy fermion systems [S20]. Thus the magnetic susceptibility, resistivity, and heat capacity all show consistent experimental signatures of non-Fermi liquid behavior in Ni_3In near zero field. We note that we may estimate the Sommerfeld-Wilson ratio R_W [S21] of the system using the magnetic susceptibility ($M_a/H_a = 7.3 \times 10^{-3}$ emu/mol) and $\gamma = 52$ mJ/mol/K^2 at 7 T, which gives rise to $R_W = \dfrac{\pi^2 k_B^2 \chi}{\mu_0 (g\mu_B)^2 \gamma} = 10.1$.

SXI. Effects of Sn-doping

In Fig. S22 we contrast the experimental powder XRD pattern of Ni_3In and Ni_3Sn used in this study. As the two materials are iso-structural (the structural prototype is Ni_3Sn), their XRD patterns are overall qualitatively similar; the difference in peak locations reflects their different lattice constants.

To further examine the role of the partially filled flat band in determining the physical properties of Ni_3In reported in the main text – (magneto-)transport, heat capacity and magnetic susceptibility – we prepared polycrystalline $Ni_3In_{1-x}Sn_x$. The characterization of these materials are summarized in Fig. S23. As shown in Fig. S23(a), the T-linear-like response in resistivity ρ observed in polycrystalline Ni_3In gives way to a conventional response in $Ni_3In_{0.9}Sn_{0.1}$ (note that ρ for the former behaves as a mixing of ρ_{ab} and ρ_c). Similarly, the specific heat normalized by temperature C_pT^{-1} for $Ni_3In_{0.9}Sn_{0.1}$ and Ni_3Sn

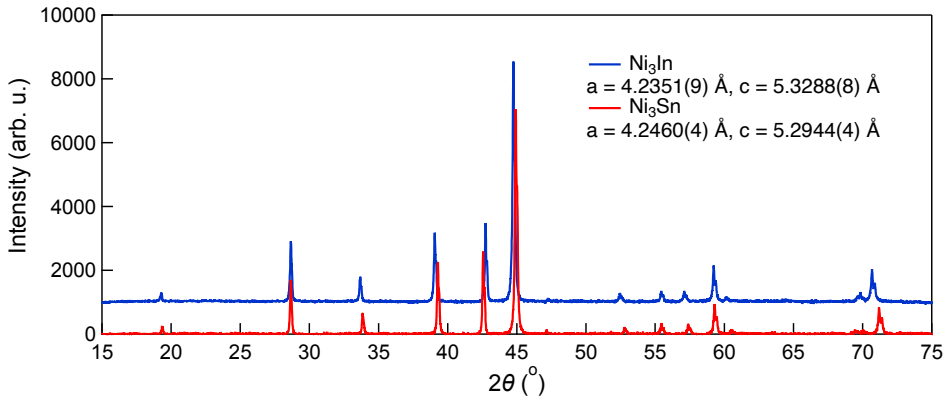

FIG. S22. **X-ray diffraction pattern of Ni_3In and Ni_3Sn** Powder XRD of Ni_3In (blue curve) and Ni_3Sn (red curve) used in this work. The respective lattice constants extracted from the peak positions are indicated in the legends.

shows the $\gamma + \beta T^2$ form expected for a Fermi liquid, while $C_p T^{-1}$ of Ni_3In at low T shows a deviation from such Fermi liquid behavior. The estimated γ of Ni_3In assuming an identical phonon contribution with $Ni_3In_{0.9}Sn_{0.1}$ is 47 mJ·K^2·mol^{-1} at the intercept of the dashed line in Fig. S23(b), approximately twice of 25 mJ·K^2·mol^{-1} for $Ni_3In_{0.9}Sn_{0.1}$ and six times of 8 mJ·K^2·mol^{-1} for Ni_3Sn. We note that although it is well-known that in quantum critical systems the nature of disorder introduced by doping may strongly influence the resulting states [S22], the observed systematic decrease of γ with increasing Sn content suggest the primary role of Sn-doping is to lift E_F away from the flat band in pristine Ni_3In.

In Fig. S23(c) we show the T-evolution of magnetic susceptibility χ for both Ni_3In and $Ni_3In_{0.9}Sn_{0.1}$, where the former exhibits a strong Curie-Weiss type increase with decreasing T, while 10% Sn doping suffices to suppress the Curie-Weiss behavior. The inset shows the x-dependence of low-T χ, where a sharp increase in χ takes place near Ni_3In ($x = 1$). This suggests that the emergence of magnetic moments/fluctuations coincides with the placement of E_F at the flat band as schematically illustrated in Fig. S23(e). Additionally, an anomalous rise in the Hall coefficient resembling the onset of a Curie-Weiss susceptibility (Fig. S23(d)) and a negative magnetoresistance (Fig. S23(d) inset) are also removed moving from Ni_3In to $Ni_3In_{0.9}Sn_{0.1}$. The behaviors shown in Fig. S23 collectively suggest a suppression of magnetic fluctuation and a recovery of a Landau Fermi liquid-like state with the introduction of electrons via Sn doping to the system. We therefore arrive at the conclusion that the

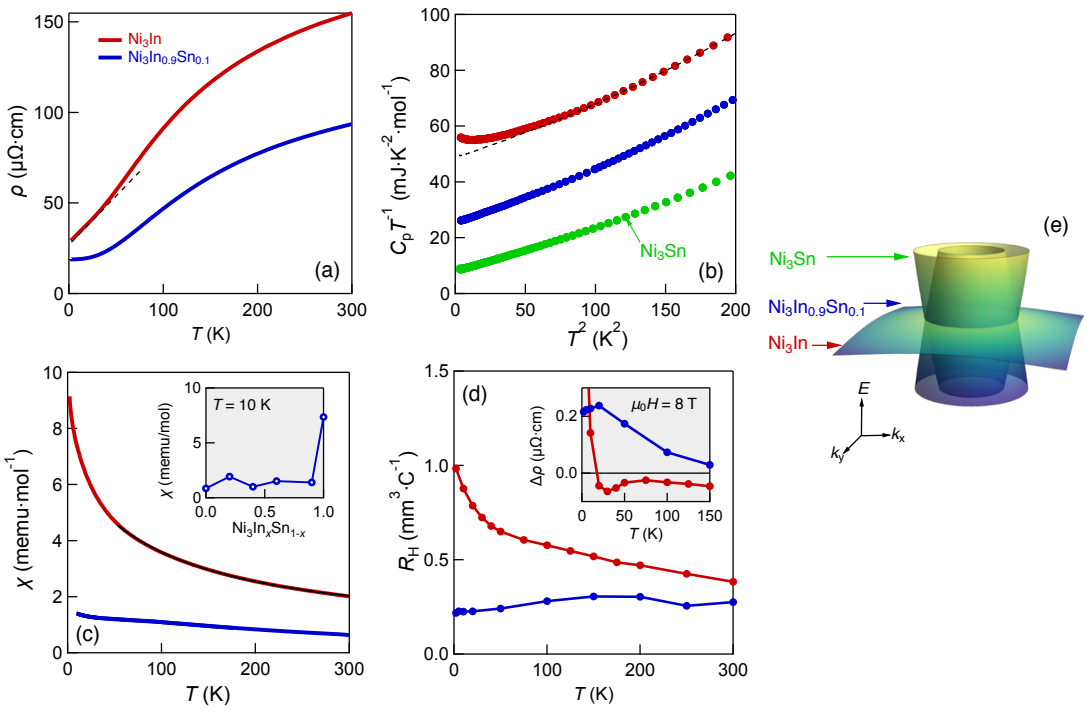

FIG. S23. **Suppression of the non-Fermi liquid behavior in Ni_3In with electron doping** (a) Resistivity of polycrystalline Ni_3In (red) and $Ni_3In_{0.9}Sn_{0.1}$ (blue). The same color scheme is adopted throughout (a-d). The dashed lines is linear in T. (b) Molar heat capacity C_p normalized by T of Ni_3In, $Ni_3In_{0.9}Sn_{0.1}$, and Ni_3Sn (green symbols). The dashed line is the response of $Ni_3In_{0.9}Sn_{0.1}$ offset to align with that of Ni_3In. (c) Magnetic susceptibility of Ni_3In and $Ni_3In_{0.9}Sn_{0.1}$. The black solid line is a Curie-Weiss fit to the high T part for Ni_3In. (d) The Hall coefficient of polycrystalline Ni_3In and $Ni_3In_{0.9}Sn_{0.1}$ as a function of temperature; the inset shows the evolution of magnetoresistance $\Delta\rho(H,T) \equiv \rho_{xx}(H,T) - \rho_{xx}(0,T)$ at 8 T with T. (e) Schematic of the electron filling of Ni_3In, $Ni_3In_{0.9}Sn_{0.1}$ and Ni_3In with respect to the flat band and the Dirac nodal ring.

stabilization and partial filling the $3d$ flat band at E_F in Ni_3In is key to the introduction of non-Fermi liquid behavior and fluctuating magnetic moments onto the kagome lattice.

[S1] Inorganic Crystal Structure Database, FIZ Karlsruhe GmbH (2019).

[S2] L. Ye, M. Kang, J. Liu, F. von Cube, C.R. Wicker, T. Suzuki, C. Jozwiak, A. Bostwick, E.

Rotenberg, D.C. Bell, L. Fu, R. Comin and J.G. Checkelsky, Massive Dirac fermions in a ferromagnetic kagome metal, Nature **555**, 638-642 (2018).

[S3] S.A. Parameswaran, A.M. Turner, D.P. Arovas and A. Vishwanath, Topological order and absence of band insulators at integer filling in non-symmorphic crystals, Nat. Phys. **9**, 299-303 (2013).

[S4] L. Fu and C.L. Kane, Topological insulators with inversion symmetry, Phys. Rev. B, **76**, 045302 (2007).

[S5] S.-Y. Yang, H. Yang, E. Derunova, S.S.P. Parkin, B. Yan and M.N. Ali, Symmetry demanded topological nodal-line materials, Adv. Phys. X **3**, 1414631 (2018).

[S6] M. Kang, L. Ye, S. Fang, J.-S. You, A. Levitan, M. Han, J.I. Facio, C. Jozwiak, A. Bostwick, E. Rotenberg, M. K. Chan, R.D. McDonald, D. Graf, K. Kaznatcheev, E. Vescovo, D.C. Bell, E. Kaxiras, J. van den Brink, M. Richter, M.P. Ghimire, J.G. Checkelsky and R. Comin, Dirac fermions and flat bands in the ideal kagome metal FeSn, Nat. Mater. **19**, 163-169 (2020).

[S7] J. Zhao, W. Wu, Y. Wang and S.A. Yang, Electronic correlations in the normal state of the kagome superconductor KV_3Sb_5, Phys. Rev. Lett. **103**, L241117 (2021).

[S8] A. Hausoel, M. Karolak, E. Şaşioğlu, A. Lichtenstein, K. Held, A. Katanin, A. Toschi and G. Sangiovanni, Local magnetic moments in iron and nickel at ambient and Earth's core conditions, Nat. Commun. **8**, 16062 (2017).

[S9] T. Moriya, Recent progress in the theory of itinerant electron magnetism, J. Magn. Magn. Mater. **14**, 1-46 (1979).

[S10] H. Yamada and S. Takada, Magnetoresistance of antiferromagnetic metals due to $s-d$ interaction. J. Phys. Soc. Jpn. **34**, 51-57 (1973).

[S11] B. Batlogg, D.J. Bishop, E. Bucher, B. Golding, A.P. Ramirez, Z. Fisk, J.L. Smith and H.R. Ott, Superconductivity and heavy fermions, J. Magn. Magn. Mater. **63,64**, 441-446 (1987).

[S12] P. Schlottmann, Bethe-ansatz solution of the ground state of the $SU(2j+1)$ Kondo (Coqblin-Schrieffer) model: magnetization, magnetoresistance and universality, Z. Phys. B Condens. Mater. **51**, 223-235 (1983).

[S13] T.A. Costi, Kondo effect in a magnetic field and the magnetoresistivity of Kondo alloys, Phys. Rev. Lett. **85**, 1504-1507 (2000).

[S14] J. Custers, P. Gegenwart, H. Wilhelm, K. Neumaier, Y. Tokiwa, O. Trovarelli, C. Geibel, F.

Steglich, C. Pépin and P. Coleman, The break-up of heavy electrons at a quantum critical point, Nature **424**, 524-527 (2003).

[S15] M.A. Susner, M. Bhatia, M.D. Sumption and E.W. Collings, Electrical resistivity, Debye temperature and connectivity in heavily doped bulk MgB_2 superconductors, J. Appl. Phys. **105**, 103916 (2009).

[S16] A.C. Jacko, J.O. Fjærestad and B.J. Powell, A unified explanation of the Kadowaki–Woods ratio in strongly correlated metals, Nat. Phys. **5**, 422-425 (2009).

[S17] R. Movshovich, A. Yatskar, M.F. Hundley, P.C. Canfield, and W.P. Beyermann, Magnetic-field dependence of the low-temperature specific heat in $PrInAg_2$: support for a nonmagnetic heavy-fermion ground state, Phys. Rev. B **59**, R6601-R6603 (1999).

[S18] G.R. Stewart, Non-Fermi-liquid behavior in $d-$ and $f-$electron metals, Rev. Mod. Phys. **73**, 797-855 (2001).

[S19] P. Coleman, Theories of non-Fermi liquid behavior in heavy fermions, Physica B **259-261**, 353-358 (1999).

[S20] Q. Si, S. Rabello, K. Ingersent and J.L. Smith, Locally critical quantum phase transitions in strongly correlated metals, Nature **413**, 804-808 (2001).

[S21] S.-I. Ikeda, Y. Maeno, S. Nakatsuji, M. Kosaka and Y. Uwatoko, Ground state in $Sr_3Ru_2O_7$: Fermi liquid close to a ferromagnetic instability, Phys. Rev. B **62**, R6089-R6092 (2000).

[S22] S. Seo, X. Lu, J.X. Zhu, R.R. Urbano, N. Curro, E.D. Bauer, V.A. Sidorov, L.D. Pham, T. Park, Z. Fisk and J.D. Thompson, Disorder in quantum critical superconductors, Nat. Phys. **10**, 120-125 (2014).